Physical modeling of direct current and radio frequency characteristics for InP-based InAlAs/InGaAs HEMTs*

Shu-Xiang Sun(孙树祥)[1], Hui-Fang Ji(吉慧芳)[1], Hui-Juan Yao(姚会娟)[1], Sheng Li(李胜)[1], Zhi Jin(金智)[2], Peng Ding(丁芃)[2], and Ying-Hui Zhong(钟英辉)[1,†]

[1] *School of Physics and Engineering, Zhengzhou University, Zhengzhou* 450001, *China*
[2] *Institute of Microelectronics, Chinese Academy of Sciences, Beijing* 100029, *China*

(Received 25 May 2016; revised manuscript received 24 June 2016; published online 25 August 2016)

Direct current (DC) and radio frequency (RF) performances of InP-based high electron mobility transistors (HEMTs) are investigated by Sentaurus TCAD. The physical models including hydrodynamic transport model, Shockley–Read–Hall recombination, Auger recombination, radiative recombination, density gradient model and high field-dependent mobility are used to characterize the devices. The simulated results and measured results about DC and RF performances are compared, showing that they are well matched. However, the slight differences in channel current and pinch-off voltage may be accounted for by the surface defects resulting from oxidized InAlAs material in the gate-recess region. Moreover, the simulated frequency characteristics can be extrapolated beyond the test equipment limitation of 40 GHz, which gives a more accurate maximum oscillation frequency ($f_{\max}$) of 385 GHz.

Keywords: InP-based HEMT, hydrodynamic model, the current gain cutoff frequency (f_{T}), the maximum oscillation frequency ($f_{\max}$)

PACS: 85.30.De, 73.61.Ey **DOI:** 10.1088/1674-1056/25/10/108501

1. Introduction

Because of high carrier sheet density, high carrier peak drift velocity and low-field mobility in InGaAs channel, InAlAs/InGaAs InP-based high electron mobility transistor (HEMT) demonstrates extremely excellent characteristics,[1–3] such as high frequency, low noise figure, and superior gain performance, and so on. Consequently, it has become a competitive candidate for various millimeter-wave circuits[4–6] and even terahertz applications.[7–9] Generally speaking, the device characteristics are closely dependent on manufacturing technologies and epitaxial structures. However, systematic technology experiments are time-consuming and costly, so alternatively, fast and accurate simulation work can be done prior to the expensive fabrication process.

Currently, a lot of reported research about HEMTs focuses on developing physical models to depict various physical phenomena, with ultimately aiming at optimizing the device performances.[10,11] Notably, most simulations are mainly concerned about direct current (DC) characteristics, such as transfer characteristic, channel current, leakage current, etc, but the frequency performances of InP-based HEMT are rarely covered. However, the current gain cutoff frequency (f_{T}) and maximum oscillation frequency ($f_{\max}$) are vitally critical parameters for high frequency applications, which greatly determine the maximum operating frequency of digital logic circuit and the power gain performance of analog circuit respectively.

In this paper, DC and radio frequency (RF) performances of InP-based HEMTs are in detail investigated by using Sentaurus TCAD. The Sentaurus Device Editor (SDE) and Sentaurus Sdevice module with reasonable physical model are used to describe the device structure and performances. Comparisons of DC and RF performances between simulation and experiment show compatible trends, which validates the proposed physical models and simulation method. This research offers an effective analytical approach for further enhancing the properties of InP-based HEMT devices.

2. Device structure and fabrication

Figure 1 shows a schematic cross-section of the InP-based HEMT. The epitaxial structure is designed and optimized by using the parameters shown in Table 1. The layers consist of an InAlAs buffer, an InGaAs channel, an unstrained InAlAs spacer layer, a Si-doped plane which provides two-dimensional electron gas (2DEG), a 12-nm-thick unstrained InAlAs Schottky barrier layer, and a composite InGaAs cap layer composed of a Si-doped InGaAs cap layer and a Si-doped $In_{0.53}Ga_{0.47}As$ transitional layer. All InAlAs layers are lattice-matched with the InP substrate.

The InP-based HEMT fabrication process is similar to that in previous work.[12,13] The mesa isolation is achieved by phosphorus acid-based wet chemical etching till $In_{0.52}Al_{0.48}As$ buffer layer. Source and drain are spaced by

*Project supported by the National Natural Science Foundation of China (Grant Nos. 61404115 and 61434006), the Postdoctoral Science Foundation of Henan Province, China (Grant No. 2014006), and the Development Fund for Outstanding Young Teachers of Zhengzhou University (Grant No. 1521317004).

†Corresponding author. E-mail: zhongyinghui@zzu.edu.cn

© 2016 Chinese Physical Society and IOP Publishing Ltd

2.4 μm through a lift-off process and then Ti/Pt/Au is evaporated by an electron beam evaporator to achieve ohmic metallization without annealing. In order to measure on-wafer DC and RF characteristics, the coplanar waveguide bond pads are formed by evaporating Ti/Au metals. In particular, the most important gate process includes gate lithography, recess, and metallization. The T-gate is determined by electron beam lithography in a trilayer of PMMA/Al/UVIII. Finally, 88 nm T-gate is obtained and located at the centre of gate-recess region.

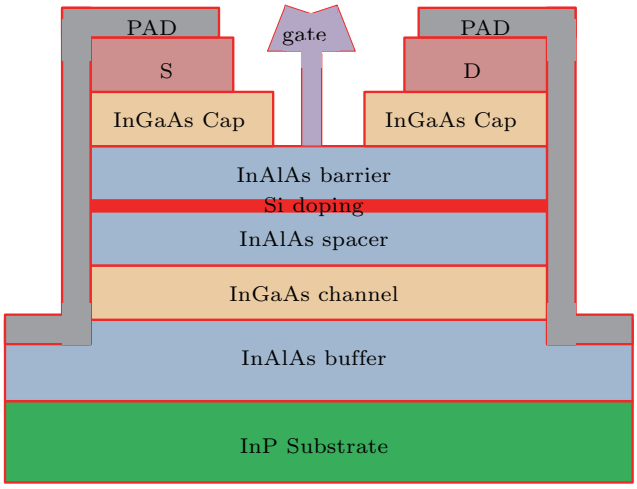


Fig. 1. (color online) Schematic cross-section of the InP-based HEMT.

Table 1. Device epitaxial layer structure.

Layer	Material	Doping	Thickness/nm
Cap layer	$In_{0.6}Ga_{0.4}As$	Si:$N^{++}3\times10^{19}$ cm^{-3}	15
Cap layer	$In_{0.53}Ga_{0.47}As$	Si:$N^{+}5\times10^{18}$ cm^{-3}	15
Barrier layer	$In_{0.52}Al_{0.48}As$	Undoped	12
Si planar-doped layer		5×10^{12} cm^{-2}	
Spacer layer	$In_{0.52}Al_{0.48}As$	Undoped	3
Channel layer	$In_{0.53}Ga_{0.47}As$	Undoped	15
Buffer layer	$In_{0.52}Al_{0.48}As$	Undoped	500
InP Substrate			

3. Simulation model

In this paper, the device structure is created by Sentaurus SDE tool. To reduce computing time and solve convergence problem, different mesh strategies are adopted in different regions. Firstly, the gradient meshing method is introduced to enhance the accuracy for key regions and reduce the number of nodes for other non-critical regions simultaneously. Secondly, sub-gridding technique is adopted to refine the key regions, including the 2DEG region, delta doping region, drain edges, gate edge, etc. Based on the actual condition, the Gaussian doping model is used in the source, drain, and delta doping layer. The device structure with mesh refinement is shown in Fig. 2. Additionally, the whole device structure is created by mirror-injection from semi-device structure, which reduces the calculating time without missing any relevant information.

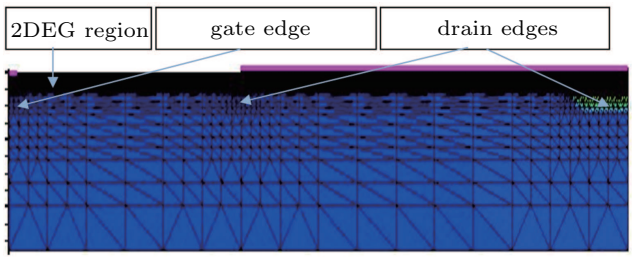


Fig. 2. (color online) Semi-device structure with mesh refinement.

Successively, electrical characteristics are simulated by using Sentaurus Device simulator, which provides various types of transport models, including hydrodynamic (HD), drift-diffusion (DD), thermodynamic (TD) and Monte Carlo models. For devices with hetero-structure, electrons can acquire very high energy and get into non-equilibrium transport condition, and therefore electron velocity can be much greater than its steady state value. However, DD simulations cannot accurately depict this non-equilibrium electron transport happening in the hetero-structure device. Admittedly, Monte Carlo method can execute accurate simulation by solving Boltzmann's transport equations, but it is time consuming and tedious. The electron and hole temperatures are not assumed to be equal to the lattice temperature in HD model, and thus energy conservation equation is additionally introduced except for Poisson equation and carrier continuity equation. Therefore, HD model precisely describes many non-equilibrium conditions such as quasi-ballistic transport in thin regions and velocity overshoot effect in depleted regions.

Besides this, several crucial physical effects are also taken into account in the simulation, including generation–recombination models, mobility models, quantum effect model, etc. Shockley–Read–Hall recombination, Auger recombination, and radiative recombination models are adopted to describe the carrier exchange process with the impurity defects in the band-gap, and the values are chosen as follows: $\tau_{\mathrm{SRH}} = 60$ ns, $C_{\mathrm{rad}} = 1.4\times10^{-9}$ cm^3/s, and $C_{\mathrm{Auger}} = 4.0\times10^{-29}$ cm^6/s.[11,14] Additionally, the density gradient model of eQuantumPotential is introduced to depict the quantum effect of 2DEG in InGaAs channel region. The parameters are obtained by linear interpolation from the parameters of AlAs, GaAs and InAs. Table 2 summarizes some important parameters adopted in the simulation, including dielectric constant (ε_{r}), effective electron mass (m_{e}), electron affinity (χ), energy gap (E_{g}), effective conduction band density of states (N_{c}), and effective valence band density of states (N_{v}).

Additionally, because of the particular band structures for InAlAs and InGaAs materials, high energy electrons will transfer into an energetically higher side valley with a much larger effective mass, and thus a negative differential mobility can be observed for high driving fields. In the present work,

Table 2. Some important parameters in the simulation.

	InAs	AlAs	GaAs
ε_r (300 K)	15.15 (static) 12.30 (high frequency)	10.06 (static) 8.16 (high frequency)	12.90 (static) 10.89 (high frequency)
m_e	$0.023m_0$	$0.71m_0$	$0.063m_0$
χ	4.90 eV	3.50 eV	4.07 eV
E_g (0 K)	0.411 eV	2.230 eV	1.519 eV
N_c	8.72×10^{16} cm^{-3}	1.5×10^{19} cm^{-3}	4.7×10^{17} cm^{-3}
N_v	6.6×10^{18} cm^{-3}	1.66×10^{19} cm^{-3}	9.0×10^{18} cm^{-3}

the transferred electron model is included in the physical models to describe the high field effect, which is given as follows:

$$\mu = \frac{\mu_{\text{low}} + (v_{\text{sat}}/F)(F/E_0)^4}{1 + (F/E_0)^4}, \tag{1}$$

where v_{sat} is the carrier peak drift velocity, F the driving electrical field, E_0 the reference field strength, and μ_{low} the carrier low-field mobility.

4. Results and discussion

In order to demonstrate the validities of the proposed physical models, the comparisons between computational curves and experimental measurement results of the devices with almost the same epitaxial structures and device dimensions are performed.

4.1. DC characteristics

Figure 3 shows the gate-bias-dependent extrinsic transconductance and channel current of InP-based HEMT at a drain–source voltage (V_{DS}) of 1.5 V. Figure 4 shows the simulated and measured drain–source current–voltage (I–V) characteristics under the gate bias (V_{GS}) varying from −0.6 V to 0 V in steps of 0.1 V. It can be observed that the trend of simulated data is consistent with that of experimental result. Particularly, the simulated channel current is detected to be apparently higher than the measured value. Besides, the experimental pinch-off voltage (V_p) and drain–source saturation current are demonstrated to be slightly higher than the corresponding simulated values.

In order to obtain high-frequency performance, no surface passivation is performed in the device fabrication process. The exposed InAlAs barrier layer can be easily oxidized, and thus many surface defects may arise on the gate-recess regions. The defect charges could modulate the electrical potential distribution in the channel region, and surface Fermi level will negatively deviate from conduction band-edge. Consequently, the increased surface potential will abate the carrier sheet density in the channel region, and thus reduce the extrinsic transconductance and channel current. Meanwhile, the additional reverse modulation may shift the pinch-off voltage towards a positive value.

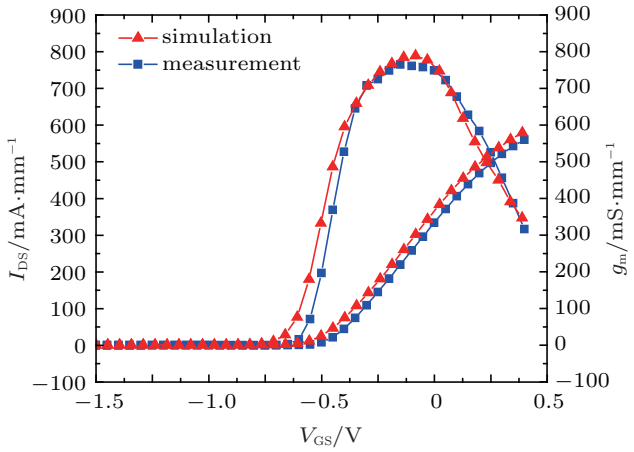


Fig. 3. (color online) Transfer characteristics of the simulated (red) and measured (blue) InP-based HEMT.

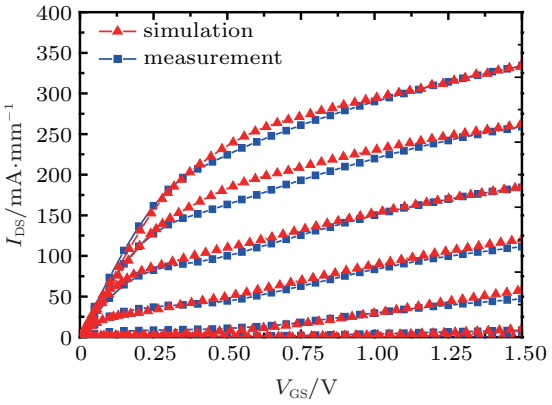


Fig. 4. (color online) I–V characteristics of the simulated (red) and measured (blue) InP-based HEMT.

4.2. RF characteristics

The f_T and $f_{\max}$ are critical parameters for high-speed applications, which can be respectively extrapolated from the current gain (H_{21}) and maximum available/stable power gain (MAG/MSG) using a least-squares fitting with a −20-dB/decade slope. In this simulation, MSG and MAG are computed from the S-parameters by Sentaurus Sdevice module through using the following equations:

$$MSG = \left|\frac{S_{21}}{S_{12}}\right|, \tag{2}$$

$$MAG = \left|\frac{S_{21}}{S_{12}}\right| \cdot (K - \sqrt{K^2 - 1}), \tag{3}$$

$$K = \frac{1 - |S_{21}|^2 - |S_{22}|^2 + |\Delta S|^2}{2|S_{12} \cdot S_{21}|}, \tag{4}$$

$$\Delta S = S_{11} \cdot S_{22} - S_{12} \cdot S_{21}, \tag{5}$$

where K is the Rollett stability factor, $K > 1$ and $\Delta S < 1$ both constitute a primary condition for the stability of the device. Figure 5 demonstrates the frequency characteristics of the simulated and measured InP-based HEMTs, which are biased at the peak transconductance points of $V_{GS} = -0.1$ V and $V_{DS} = 1.75$ V. The measured f_T and f_{max} are extrapolated to be 150 GHz and 201 GHz, which are improved to be 165 GHz and 385 GHz for simulation. Notably, the simulated and measured gain performances go downward theoretically as frequency increases with a slope of -20 dB/decade. Moreover, S-parameters of the InP-based HEMT are measured over frequencies from 0.1 GHz up to 40 GHz in steps of 0.1 GHz. However, the device is still potentially unstable ($K < 1$) at the instrumentation limit of 40 GHz, therefore, extrapolating the gain at this point with the -20-dB/decade slope indicates a real f_{max} more than 201 GHz. Consequently, the simulation compensates partly for the limitation of test equipment, and gives a more accurate f_{max} of 385 GHz.

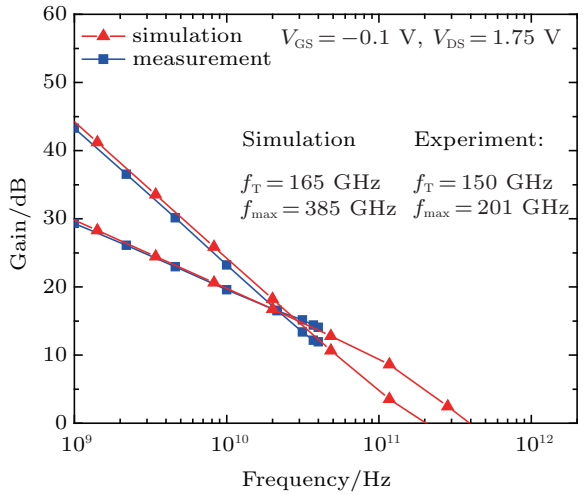


Fig. 5. (color online) Frequency characteristics of the simulated (red) and measured (blue) InP-based HEMT.

5. Conclusions

In this paper, DC and RF performances of InP-based HEMTs are investigated by Sentaurus TCAD. The device structure is established by SDE module, moreover, the gradient meshing and sub-gridding technique are adopted in different regions to reduce computing time and solve the convergence problem. The 2D electrical simulation is performed by using Sentaurus Device simulator. The physical models including HD transport model, Shockley–Read–Hall recombination, Auger recombination, radiative recombination, density gradient model, and high field-dependent mobility are used to characterize the devices. The simulated results and measured results about the DC and RF characteristics have compatible trends, which confirms the validities of the proposed models and simulation method. Further, three-dimensional simulation may be performed to give a more accurate description of InP-based HEMT. However, the achievements of this research offer an effective analytical approach for further enhancing the properties of InP-based HEMT devices.

Acknowledgment

The authors would like to express their heartfelt thanks to Lu Bin and Liu Min from Xi Dian University for guidance in the operation of Sentaurus TCAD software.

References

[1] Wang L D, Ding P, Su Y B, Chen J, Zhang B C and Jin Z 2014 *Chin. Phys. B* **23** 038501
[2] Li H O, Huang W, Tang CW, Deng X F and Lau K M 2011 *Chin. Phys. B* **20** 068502
[3] Huang J, Li M, Zhao Q, Gu W W and Lau K M 2015 *Chin. Phys. B* **24** 087035
[4] Deal, W R, Mei X B, Radisic V Leong K, Sarkozy S, Gorospe B, Lee J, Liu P H, Yoshida W, Lange M, Uyeda J and Lai R 2010 *IEEE Microwave and Wireless Components Letters* **20** 289
[5] Liu L, Alt A R, Benedickter H and Bologenesi C R 2011 *IEEE MTT-S International Microwave Workshop Series on Millimeter Wave Integration Technologies (IMWS),* September 15–16, 2011, Sitges Barcelona pp. 9–12
[6] Radisc V, Leong K M, Mei X B, Sarkozy S, Yoshida W, Liu P H, Uyeda J and Beach W 2010, *IEEE MTT-S International Microwave Symposium Digest (MTT)*, May 23–28, 2010 Anaheim, California, USA, pp. 45–48
[7] Deal W, Mei X B, Leong K M K H, Radisic V, Sarkozy S and Lai R 2011 *IEEE Trans. Terahertz Sci. Technol.* **1** 25
[8] Deal W R, Radisic V, Scott D and Mei X B 2010 *IEEE MTT-S International Microwave Symposium Digest,* May 23–28, 2010, Anaheim, California, USA, p. 1
[9] Deal W R, Leong K, Zamora A, Radisic V and Mei X B 2014 *IEEE MTT-S International Microwave Symposium (IMS)*, June 1–6, 2014, Tampa, Florida, USA, pp. 1–3
[10] Ahmad M, Butt H T, Tauqeer T and Missous M 2012 *The 9th International Conference on Advanced Semiconductor Devices and Microsystems*, November 11–15, 2012, Smolenice, Slovakia, pp. 187–190
[11] Pati S K, Pardeshi H, Raj G, Kumar N M and Sarkar C K 2013 *Superlattices and Microstructures* **55** 8
[12] Zhong Y H, Zhang Y M, Zhang Y M, Wang X T, Lv H L, Liu X Y and Jin Z 2013 *Chin. Phys. B* **22** 128503
[13] Zhong Y H, Yang J, Li X J, Ding P and Jin Z 2015 *J. Korean Phys. Soc.* **66** 1020
[14] Ge J, Liu H G, Su Y B, Cao Y X and Jin Z 2012 *Chin. Phys. B* **21** 058501